Asian Journal of Chemistry; Vol. 38, No. 11 (2026), 3011-3020
ASIAN JOURNAL OF CHEMISTRY
https://doi.org/10.14233/ajchem.2026.37000

Dielectric and Triboelectric Properties of Strontium- and Fluorine-Doped Nanohydroxyapatites

R.L. SINDHU[1,2,*], SINI CHANDRAN[1] and V.M. ANANDAKUMAR[1]

[1]Department of Physics, Mahatma Gandhi College, Thiruvananthapuram-695004, India
[2]Department of Physics, University College, Thiruvananthapuram-695034, India

*Corresponding author: E-mail: sindhuajai8@gmail.com

Received: 11 August 2026 *Accepted*: 9 October 2026 *Published online*: 13 November 2026 AJC-22532

This study investigates the effects of independent strontium and fluorine substitution on the dielectric behaviour and preliminary triboelectric performance of chemically synthesized nanohydroxyapatite. X-ray diffraction confirmed the hexagonal crystal structure, while Fourier-transform infrared spectroscopy verified the characteristic bonding features of the material. Dielectric measurements across a broad frequency range revealed different responses to the two dopants. Strontium-substituted samples exhibited higher dielectric constants at low frequencies, which may be associated with lattice distortion and enhanced space-charge polarization. Fluorine substitution resulted in lower dielectric loss and higher electrical stability, which is consistent with reduced defect-related dipolar relaxation. In preliminary triboelectric tests, doped nanohydroxyapatite incorporated into a polymer matrix yielded higher electrical output during repeated contact-separation cycles. The findings establish a basis for exploring ionic substitution as a means of tuning nanohydroxyapatite for dielectric and triboelectric applications.

Keywords: Hydroxyapatite, Bio-ceramic, Triboelectric nanogenerator, Polyvinyl alcohol.

INTRODUCTION

Nanostructured materials have attracted significant attention due to their tunable electrical, dielectric and surface properties, which are highly desirable for advanced electronic and energy-harvesting applications [1]. Among these materials, hydroxyapatite (HA), $Ca_{10}(PO_4)_6(OH)_2$, has been extensively studied due to its chemical stability, structural flexibility and excellent compatibility with biological systems [1]. Although hydroxyapatite has traditionally been used in orthopaedic and dental applications, recent investigations indicate that nano-scale hydroxyapatite can also be used in electronic, opto-electronic and energy-harvesting devices owing to its dielectric behaviour and charge-storage capability [2]. A distinctive feature of hydroxyapatite is its ability to accommodate a wide range of ionic substitutions within its crystal lattice without altering the fundamental apatite framework [3,4]. The systematic incorporation of foreign ions at calcium or hydroxyl sites alters structural, electrical and surface properties, thereby modifying the functional performance of hydroxyapatite-based materials [4,5]. Among the various substituting ions, strontium (Sr^{2+}) and fluoride (F^-) have received considerable attention because of their ionic similarity with calcium (Ca^{2+}) and hydroxyl (OH^-) ions, respectively [3,4]. These structural modifications are expected to play a significant role in influencing dielectric dispersion behaviour and energy dissipation processes in hydroxyapatite-based materials [1,4].

Triboelectric nanogenerators (TENGs) generate electrical power by converting mechanical energy into electricity through the coupling of triboelectrification and electrostatic induction mechanisms [6]. The electrical output performance of a TENG depends strongly on the physical and chemical characteristics of the triboelectric materials, particularly their surface charge density and dielectric properties [7]. One effective strategy to enhance the electrical output of polymer-based TENGs is to incorporate ceramic nanofillers with relatively high dielectric constants, thereby improving charge storage and polarization within the composite layer [8]. Among such ceramic fillers, nanohydroxyapatite has attracted attention due to its dielectric properties can be tuned through controlled ionic substitution within the apatite lattice [4].

Previous studies [9,10] reported that Sr^{2+} substitution alters HA lattice parameters, while F^- incorporation reduces lattice dimensions and crystallite size [11,12]. Low fluoride

This is an open access journal, and articles are distributed under the terms of the Attribution 4.0 International (CC BY 4.0) License. This license lets others distribute, remix, tweak, and build upon your work, even commercially, as long as they credit the author for the original creation. You must give appropriate credit, provide a link to the license, and indicate if changes were made.

content was selected to limit potential adverse effects associated with excessive fluoride incorporation [13]. The 1 mol% F^- content also allowed measurable contraction of the *a*-axis. This study focusses on the effect of doping on the dielectric behaviour of nanohydroxyapatite and explores its suitability as a ceramic filler in TENGs for energy harvesting and electronic applications. Hence, in the present study, nanohydroxyapatite (HAp) was prepared chemically and subsequently doped with strontium (Sr^{2+}) and fluoride (F^-) ions to induce structural and dielectric modifications. Ionic substitution of Ca^{2+} with Sr^{2+} introduces lattice distortion due to the larger ionic radius of strontium, which can influence polarization behaviour and enhance space-charge effects within the hydroxyapatite structure [2,14]. Similarly, the substitution of hydroxyl ions with fluorine leads to the formation of fluorapatite with improved crystallinity and reduced lattice defects, thereby influencing dielectric behaviour and charge storage characteristics [3,15]. The Sr^{2+} and F^- doping concentrations were fixed at 2 and 1 mol%, respectively, to preserve the apatite structure and minimize secondary-phase formation. As only one concentration of each dopant was investigated, the findings establish their effects at these specific levels relative to pure hydroxyapatite, without determining concentration-dependent behaviour or an optimum composition.

EXPERIMENTAL

Nanohydroxyapatite were prepared by chemical precipitation of calcium nitrate tetrahydrate ($Ca(NO_3)_2{\cdot}4H_2O$, Merck) and diammonium hydrogen phosphate ($(NH_4)_2HPO_4$, Merck) at pH 9. Ammonium hydroxide (99%) was added to maintain the solution at pH 9. Ammonium fluoride and strontium nitrate anhydrous were used to produce fluorine and strontium doping. Hydrochloric acid, polytetrafluoroethylene (PTFE) tape and copper-clad electrodes were used for fabricating triboelectric layers. Polyvinyl alcohol (PVA) with an average molecular weight of 85000-124000 g mol^{-1} and a degree of hydrolysis of ≥ 98% was used as the polymer matrix.

Synthesis of pure and doped nanohydroxyapatite: Nanohydroxyapatite (HA) was synthesized by wet chemical precipitation [16-18] using aqueous calcium nitrate and diammonium hydrogen phosphate solutions at a Ca/P molar ratio of 1.67. The phosphate solution was added dropwise to the calcium nitrate solution under continuous stirring, while the pH was maintained at 9 using aqueous ammonia. After an additional 1 h of stirring, the mixture was aged for 18 h. The precipitate was collected by centrifugation, washed repeatedly with deionized water, dried at 80 ºC for 16 h and ground into a fine powder. Strontium- and fluoride-substituted samples (SrHA and FHA, respectively) were prepared using the same procedure, with strontium nitrate and ammonium fluoride added in appropriate proportions to maintain the cation-to-phosphorus molar ratio at 1.67 [19-22].

Characterization: The crystalline structure was examined by powder X-ray diffraction (XRD) using a Bruker D8 ADVANCE diffractometer with DAVINCI design, operated at 30 kV and 10 mA with Cu*K*α radiation (λ = 1.5418 Å). Data were collected over 2θ = 10-79º with a step size of 0.02º and the average crystallite size was determined. Functional groups were identified by FTIR spectroscopy using a Thermo Scientific Nicolet iS50 over 4000-400 cm^{-1} with KBr pellets. Thermal behaviour was assessed using a Perkin-Elmer STA 8000 thermogravimetric analyzer. Elemental composition was examined by energy-dispersive X-ray spectroscopy (EDS) using a Carl Zeiss EVO 18 Research instrument. Specific surface area was measured using an Anton Paar NOVAtouch 4LX-1 BET analyzer after degassing the samples at 120 ºC for 2 h. Dielectric properties were evaluated at room temperature by broadband dielectric spectroscopy using a Concept 80 system (NOVOCONTROL Technologies GmbH & Co., Germany) over 1 Hz-1 MHz.

Fabrication of positive triboelectric layers: The triboelectric performance of pure and doped hydroxyapatite was evaluated by fabricating them as positive triboelectric layers. A PVA solution was first prepared by dissolving 1 g of PVA powder in 15 mL of deionized water under continuous magnetic stirring at 75 ºC for 1 h. For the fabrication of HA12.5 layer, hydroxyapatite powder was incorporated into the PVA solution at 12.5 wt.% (relative to the PVA content) and the resulting mixture was coated onto pre-cleaned, etched copper clad electrodes. The coated electrodes were subsequently dried at room temperature for 24 h [23-26]. The remaining triboelectric layers were fabricated following the same procedure. Accordingly, three sets of positive triboelectric layers (HA, SrHA and FHA) were obtained by incorporating 12.5 wt.% of pure, Sr-doped and F-doped hydroxyapatite, respectively, into the PVA matrix. For the negative triboelectric layer, PTFE tape was wrapped uniformly around copper-clad plates.

Measurement of electrical output: The fabricated positive and negative triboelectric layers were mounted on an in-house-developed triboelectric testing setup and operated in vertical contact-separation mode. The mechanism was driven at a contact frequency of 1 Hz, enabling periodic contact and separation between the two layers. The output signals from the fabricated TENG were recorded using a Keithley 2450 sourcemeter [26].

RESULTS AND DISCUSSION

XRD studies: The XRD patterns recorded for the pure and doped hydroxyapatite samples are shown in Fig. 1. The XRD pattern of nanohydroxyapatite (Fig. 1) matched the hexagonal apatite phase (ICDD No. 09-0432), with characteristic peaks at 2θ values of ≈ 25.9º, 31.7º, 32.2º and 32.9º, corresponding to the (002), (211), (112) and (300) planes, respectively [27,28]. The absence of additional diffraction peaks supports the formation of phase-pure HA [2]. The Scherrer equation yielded crystallite sizes of 20.2 nm for HA, 22.1 nm for SrHA and 13.86 nm for FHA. The slight increase in crystallite size after Sr^{2+} substitution may be associated with the larger ionic radius of Sr^{2+} (1.12 Å) compared with Ca^{2+} (0.99 Å), which can expand the lattice and alter crystal growth kinetics [2,29-31].

A decrease in crystallite size to 13.86 nm was observed for fluoride-doped hydroxyapatite. The smaller crystallite size of FHA compared with pure HA (Table-1) may be attributed to the replacement of OH^- ions by the smaller and more electronegative F^- ions in the apatite lattice [11,32]. This sub-

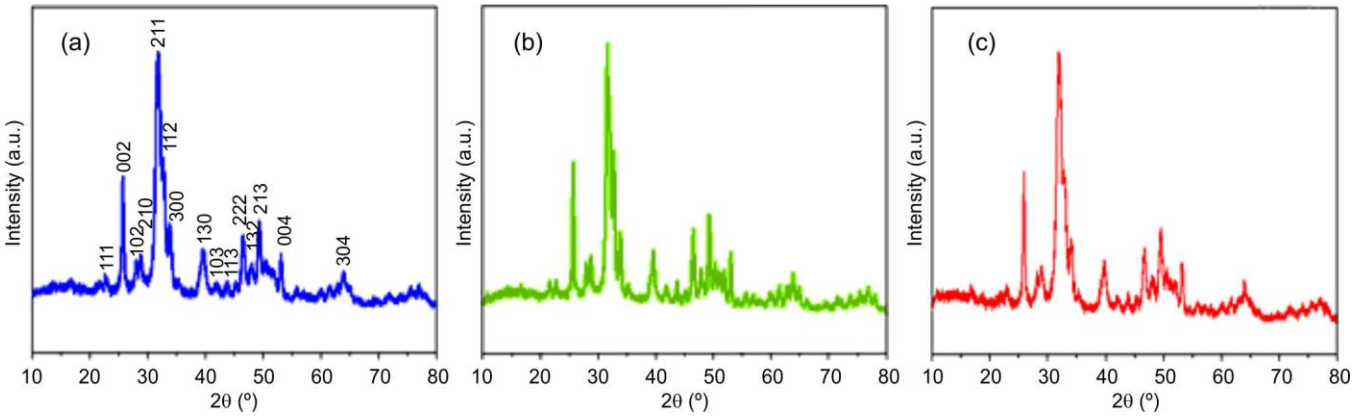


Fig. 1. XRD patterns of (a) pure hydroxyapatite, (b) strontium doped hydroxyapatite and (c) fluorine doped hydroxyapatite

TABLE-1
LIST OF CRYSTALLITE SIZE, LATTICE PARAMETERS AND UNIT CELL VOLUME OF SAMPLES

Sample	Crystallite size (nm)	Lattice constant (Å)		Unit cell volume (Å^3)
		a	*c*	
HA	20.211	9.433	6.884	530.44
SrHA	22.112	9.442	6.896	532.32
FHA	13.326	9.413	6.885	528.27

stitution produces lattice contraction and alters the kinetics of crystal growth in such a way as to reduce excessive grain growth and allow for the formation of smaller crystallites [33,34]. Rietveld refinement (Fig. 2) gave good agreement between observed and calculated patterns (χ^2 = 1.308, 1.99 and 1.79 for HA, SrHA and FHA, respectively. Relative to HA, Sr doping expanded both lattice constants (Δa = +0.009 Å, Δc = +0.012 Å; ΔV = +1.88 Å^3, +0.35%), which is consistent with the larger ionic radius of Sr^{2+} (1.18 Å) replacing Ca^{2+} (1.00 Å) [35,36]. In FHA, the *a*-axis contracted (Δa = -0.020 Å) while '*c*' was essentially unchanged (Δc = +0.002 Å), giving a volume reduction of 0.41%, which is characteristic of F^- occupying the OH^- channel sites [11]. Table-1 lists the lattice constants and unit cell volume. Compared with HA, the reflections of SrHA shift slightly toward lower 2θ, which indicate larger interplanar spacing and consistent with the larger Sr^{2+} ion (1.18 Å) replacing Ca^{2+} (1.00 Å) in the apatite lattice [35]. The reflections of FHA shift slightly toward higher 2θ, as expected when the smaller F^- ion enters the channel sites and draws the structure together along the *a*-axis, a pattern previously described for fluoride-doped hydroxyapatites [32,37].

FT-IR studies: The characteristic vibrational bands of the apatite structure are present in the FTIR spectra of pure hydroxyapatite (HA), 1 mol% fluoride-doped hydroxyapatite (FHA) and 2 mol% strontium-doped hydroxyapatite (SrHA) (Fig. 3). The strong absorption bands observed in the region of ~1090-1030 and ~962 cm^{-1} correspond to the asymmetric and symmetric stretching vibrations of PO_4^{3-} groups, respectively [17,38]. In addition, the peaks located at ~602 and 565 cm^{-1} are assigned to the bending modes of phosphate (PO_4^{3-}), which are characteristic vibrational features of crystalline hydroxyapatite [2,17]. The presence of these bands confirms the formation of the apatite phase. The broad absorption band

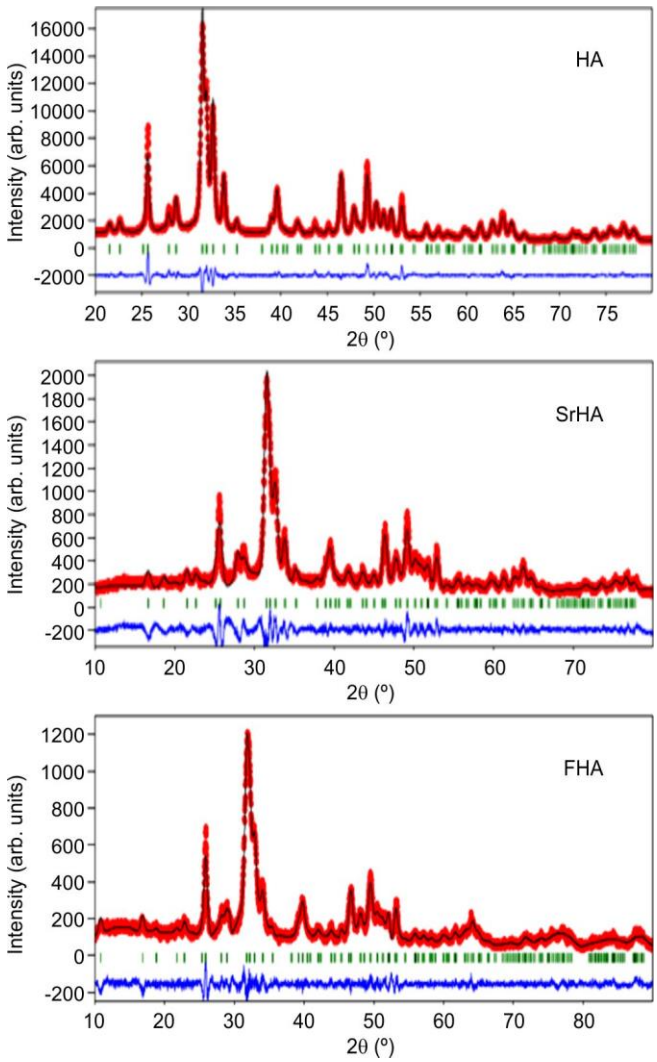


Fig. 2. Rietveld refinement profiles of the synthesized HA, SrHA and FHA powders

around ~3400 cm^{-1} and the peak near ~1630 cm^{-1} are attributed to adsorbed water molecules and H–O–H bending vibrations present on the surface of the hydroxyapatite crystals [39,40]. All characteristic FTIR bands associated with the apatite structure remain present in both doped samples, which indicate that doping does not alter the fundamental hydroxy-

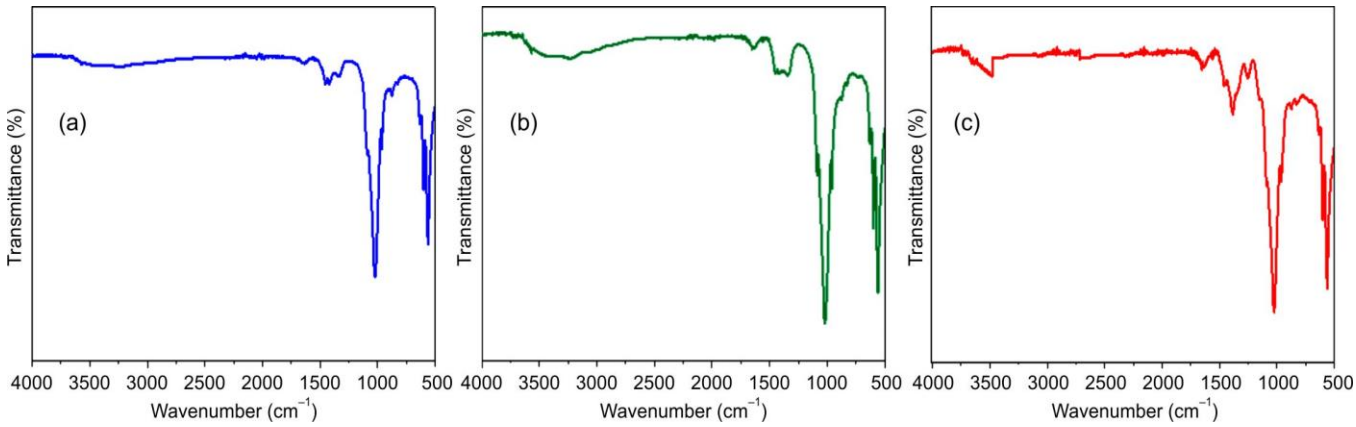


Fig. 3. FTIR spectra of (a) pure hydroxyapatite, (b) strontium doped hydroxyapatite and (c) fluorine doped hydroxyapatite

apatite crystal structure. Weak bands at ~1450-1420 and ~875 cm^{-1} are due to the presence of trace carbonate (CO_3^{2-}), which is consistent with the Ca/P ratio of pure HA (~1.78) being above the stoichiometric value of 1.67 [41-43]. The PO_4^{3-} bands of SrHA and FHA lie within approximately 3 cm^{-1} of those of pure HA. No clear shift or broadening of the phosphate bands was detected, supporting the retention of the HA framework at the selected doping levels. The OH^- stretching band near 3570 cm^{-1} is weak in all samples and nearly absent in FHA, consistent with the partial substitution of OH^- by F^- ions [37].

Thermal studies: Thermogravimetric (TG) analysis was carried out to evaluate the thermal stability of pure hydroxyapatite (HA), 2 mol% strontium-doped hydroxyapatite (SrHA) and 1 mol% fluorine-doped hydroxyapatite (FHA) (Fig. 4). The TG curves recorded from room temperature to 800 ºC show stepwise mass loss in all three samples. The initial loss below 150 ºC is mainly associated with the removal of surface-adsorbed water [44]. Mass loss between 150 and 400 ºC may arise from the removal of bound water and the decomposition of residual organic species from the precipitation process [45]. Above 400 ºC, the gradual mass loss is attributed mainly to partial dehydroxylation of the HA structure [45,46]. SrHA exhibited the highest mass loss of 9.3% compared with 8.3% for pure HA. This difference may be linked to lattice expansion and distortion following the substitution of Ca^{2+} by larger Sr^{2+} ions [47]. FHA showed the lowest mass loss at 6.1% which is consistent with improved thermal stability arising from the replacement of OH^- groups by F^- ions. This substitution strengthens the lattice and limits dehydroxylation at elevated temperatures [48]. The TG results confirm that all samples retain considerable thermal stability up to 800 ºC with fluoride substitution improving thermal resistance while strontium substitution slightly increases mass loss.

Morphological studies: Energy dispersive X-ray spectroscopy (EDS) analysis confirms the HA, 2 mol% SrHA and 1 mol% FHA (Fig. 5). The pure HA sample shows the presence of Ca, P and O elements, verifying the formation of calcium phosphate, with a Ca/P atomic ratio of about 1.78, which is close to the stoichiometric value of hydroxyapatite (Ca/P ≈ 1.67) reported in the literature [49-51]. In the SrHA sample, the (Ca+Sr)/P ratio (~1.73) indicates that the hydroxyapatite crystal structure is retained after doping [52-54]. In the FHA

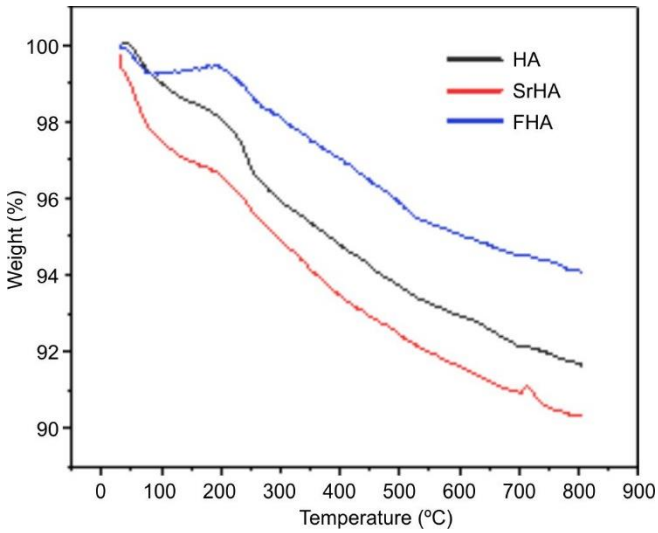


Fig. 4. Thermograms of (a) pure hydroxyapatite, (b) strontium-doped hydroxyapatite and (c) fluorine-doped hydroxyapatite

sample, the presence of a small amount of F and a Ca/P ratio (~1.65**)** is close to the theoretical value expected for hydroxyapatite-based structures [55-58]. The Ca/P molar ratio of pure HA obtained from EDS was ~1.78 (Fig. 5), which is higher than the stoichiometric value of 1.67 [33]. This deviation is attributed mainly to the presence of carbonate (CO_3^{2-} replacing PO_4^{3-}), which is evident from the FTIR bands at ~1450–1420 and ~875 cm^{-1} (Fig. 3) and is known to raise the Ca/P ratio of hydroxyapatites above 1.67 [41,42]. Carbonate is readily incorporated from atmospheric CO_2 during precipitation at high pH. The XRD patterns show no reflections of secondary phases such as CaO or $Ca(OH)_2$, so the excess Ca is not ascribed to a separate calcium-rich phase. The (Ca + Sr)/P ratio of SrHA (~1.73) and the Ca/P ratio of FHA (~1.65) are closer to the stoichiometric value. TEM images show that the morphology of the samples was rod-shaped. The mean particle size were 21.09 ± 1.3 nm, 23.62 ± 1.36 nm and 13.19 ± 1.27 nm for HA, SrHA and FHA, respectively (Fig. 6).

BET studies: The BET analysis (Fig. 7) revealed type IV isotherms for HA and its Sr- and F-doped variants. This profile is characteristic of mesoporous materials [46]. Pure HA exhibited a specific surface area of 82 m^2/g with a total pore volume of 0.70 cm^3/g and an average pore radius of

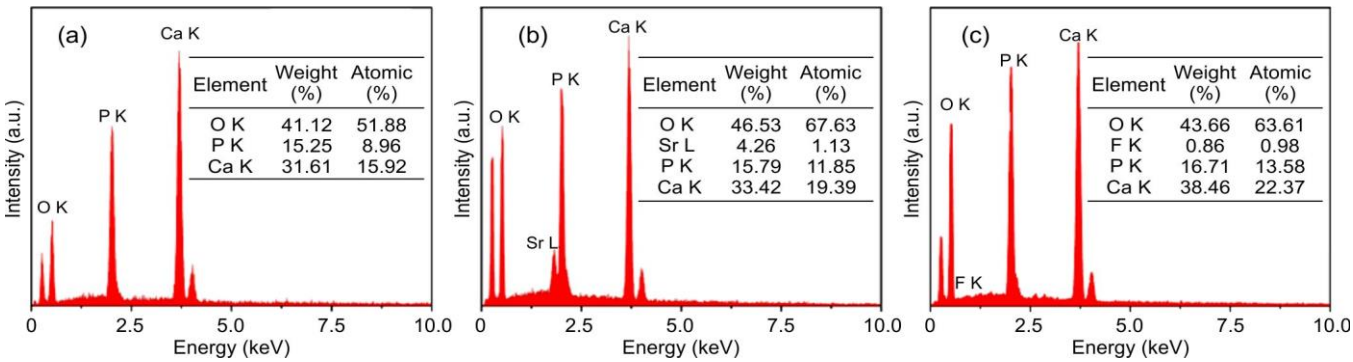


Fig. 5. EDS spectra of (a) pure hydroxyapatite, (b) strontium-doped hydroxyapatite and (c) fluorine-doped hydroxyapatite

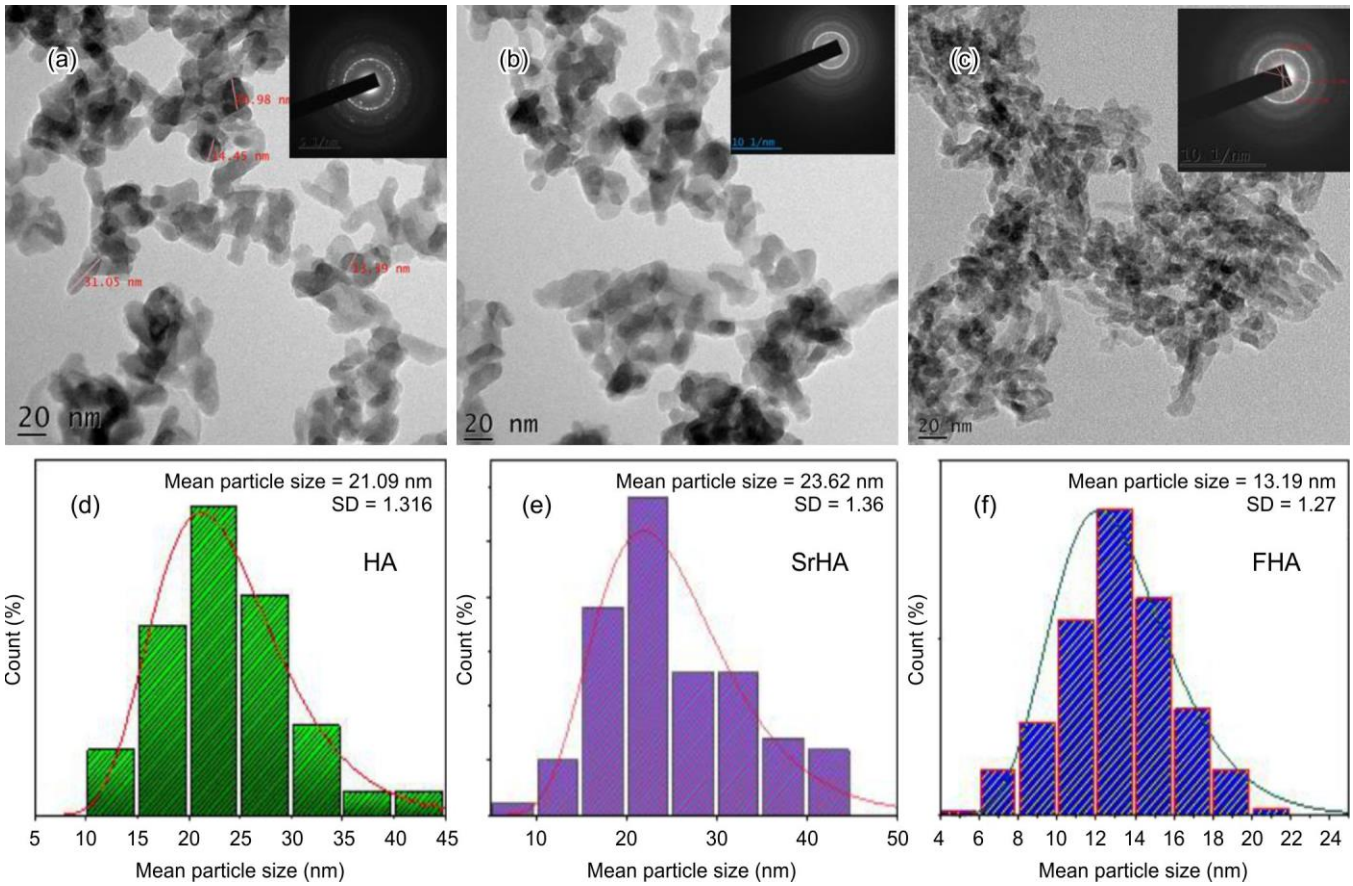


Fig. 6. (a-c), HRTEM images of HA, SrHA, FHA and SAED patterns (d-f) illustrate the corresponding particle size distribution obtained from HRTEM measurements

9.748 nm. These values are consistent with previously reported mesoporous nano-HA systems [59]. SrHA showed a lower surface area of approximately 76 m^2/g and a pore volume of 0.41 cm^3/g with an average pore size of 9.08 nm. The reduced surface area may be associated with enhanced grain growth and partial pore elimination following Sr substitution [60]. FHA exhibited the highest surface area of 84 m^2/g despite having the lowest pore volume of 0.31 cm^3/g and an average pore radius of approximately 7.5 nm. This combination may arise from changes in pore dimensions and structural ordering following fluoride substitution [61]. The BET parameters are listed in Table-2. All samples showed linear multipoint BET plots with an R^2 value of 0.9999. The changes in surface area and pore characteristics following doping may influence the suitability of these materials as ceramic fillers for energy-related applications.

Dielectric properties: The frequency-dependent dielectric properties such as dielectric constant (ε′), dielectric loss (ε″), loss tangent (tan δ), AC conductivity (σ_{ac}) and capacitance (Fig. 8) of HA, SrHA and FHA were measured. The dielectric constant of the samples HA, SrHA and FHA at 1 Hz was 23565, 40448 and 64624, respectively. At 1 kHz, the values were 135, 400 and 523 and at 1 MHz, 12, 16 and 17, respectively. The dielectric constant of all samples decreases sharply with increasing frequency. At low frequencies, all types of polarization mechanisms (electronic, ionic, dipolar and space

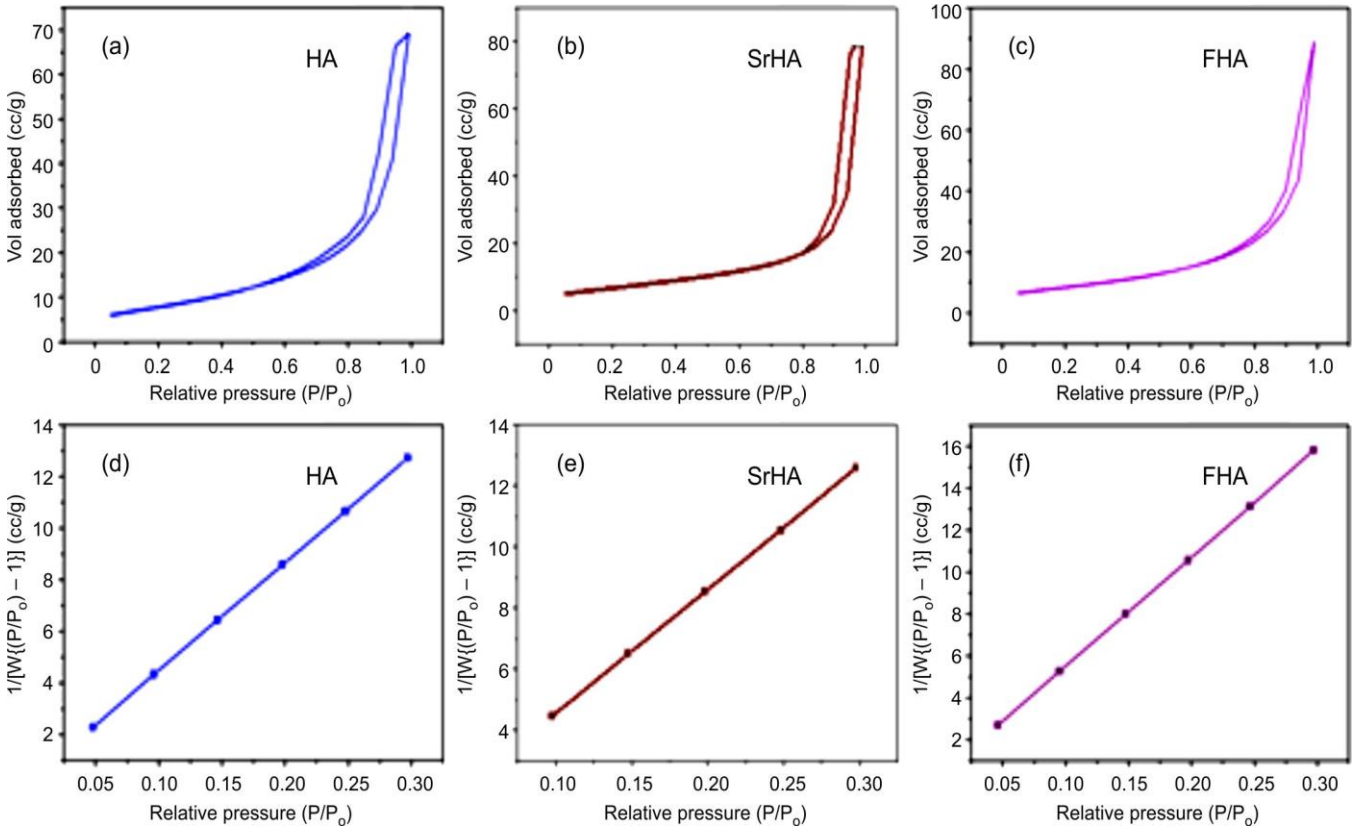


Fig. 7. BET isotherms of (a) pure hydroxyapatite, (b) strontium doped hydroxyapatite and (c) fluorine doped hydroxyapatite bet multi-point plot for (d) pure hydroxyapatite, (e) strontium doped hydroxyapatite and (f) fluorine doped hydroxyapatite

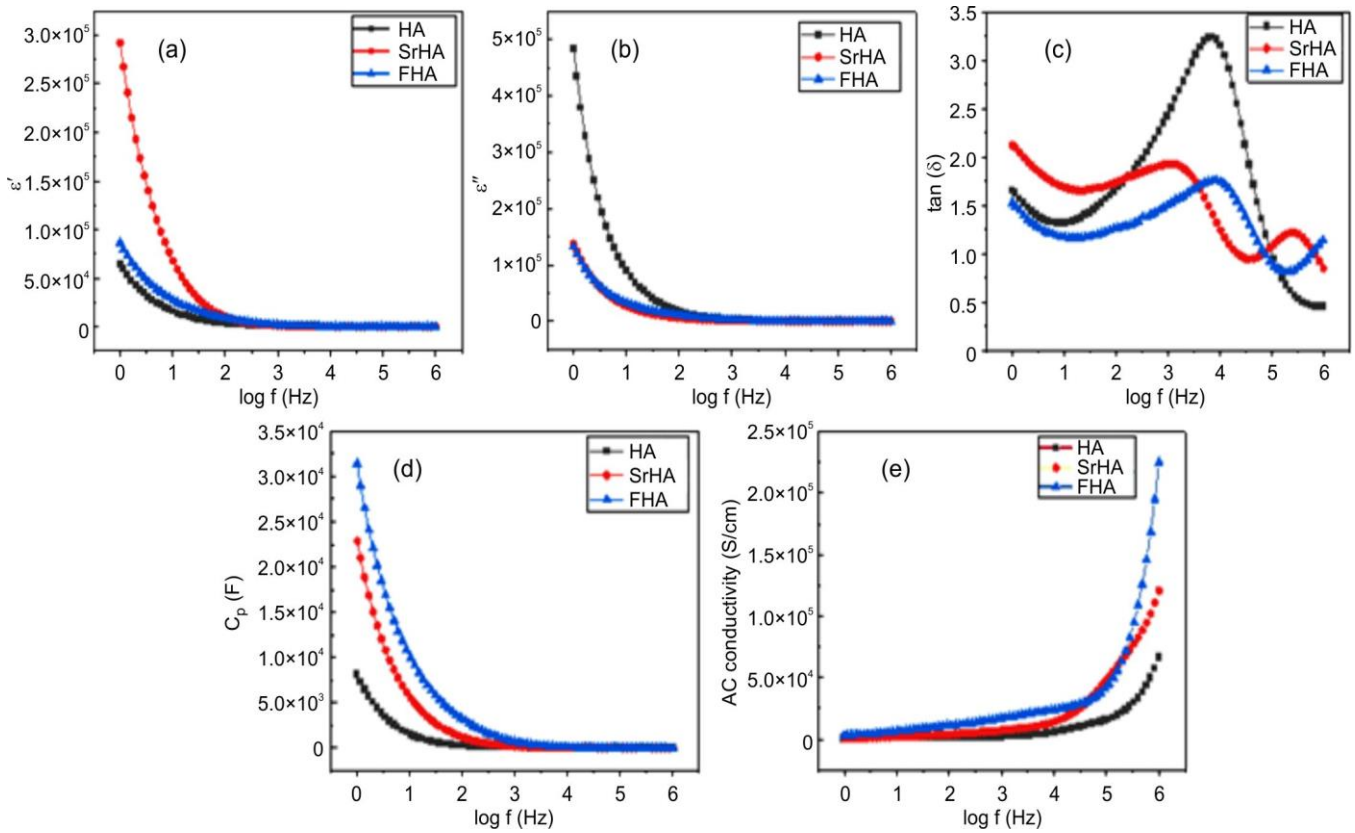


Fig. 8. Plots of the (a) dielectric constant (ε′), (b) dielectric loss (ε″), (c) loss tangent (tan δ), (d) AC conductivity (σ_{ac}) and (e) capacitance (C_p) of the samples as a function of log f

TABLE-2
COMPARISON OF BET SURFACE AREA, PORE VOLUME AND PORE RADIUS FOR HA, SrHA AND FHA SAMPLES

Sample	BET surface area (m^2/g)	Total pore volume (cm^3/g)	Average pore radius (nm)	Isotherm type
HA	82	0.7	9.748	Type IV (mesoporous)
SrHA	76	0.41	9.08	Type IV (mesoporous)
FHA	84	0.3142	7.5931	Type IV (mesoporous)

charge polarization) contribute to a large value of the dielectric constant. As frequency increases the slower polarization mechanisms become unable to follow the alternating electric field. Space-charge polarization decreases first followed by dipolar polarization as the dipoles cannot reorient rapidly enough. This leads to a decrease in the dielectric constant with increasing frequency. At higher frequencies electronic and ionic polarization remain the dominant contributions and the dielectric constant approaches a nearly constant value [62]. Sr doping increases the dielectric constant and this change may be associated with lattice distortion caused by the substitution of Ca^{2+} with larger Sr^{2+} ions. Such structural changes can modify ionic displacement and enhance the polarization response under an applied electric field [63-65]. FHA exhibits a higher dielectric constant which may be linked to the substitution of OH^- by smaller and more electronegative F^- ions. Fluoride incorporation contracts the lattice and alters the local electrostatic environment around calcium ions. The changes in the orientation of the remaining OH^- groups and local dipolar interactions may contribute to the enhanced dielectric response [64,66,67]. At low frequencies SrHA exhibited a higher dielectric constant than HA and FHA. This behaviour may arise from local lattice distortions caused by the substitution of Ca^{2+} with larger Sr^{2+} ions. The resulting defects may promote charge accumulation at grain boundaries and enhance interfacial polarization in accordance with the Maxwell-Wagner model. HA and FHA showed a lower dielectric response in this frequency range. At high frequencies, the dielectric constants of all three samples approached similar values as the slower polarization mechanisms became unable to follow the rapidly alternating electric field. The remaining response is governed mainly by faster polarization processes within the material [63,64].

The dielectric loss (ε′′) decreased with increasing frequency for all samples. At 1 Hz the values for HA and SrHA and FHA were 483287 and 137298 and 132000 respectively. At 1 kHz the corresponding values were 864, 639 and 284, whereas at 1 MHz they decreased to 46 and 17 and 14. The high loss at low frequencies may arise from interfacial polarization and charge-carrier hopping at defect sites and grain boundaries where mobile charges can respond to the applied field [63,68]. These processes become less effective at higher frequencies as the field changes too rapidly for charge accumulation and carrier movement. HA exhibited greater low-frequency loss than SrHA and FHA. This difference may be linked to changes in defect chemistry and grain-boundary conduction following Sr^{2+} and F^- substitution. The loss values became closer at high frequencies where slower polarization mechanisms contribute less to the response [66,69].

The tan δ curves exhibited relaxation peaks in the intermediate frequency region. These peaks may be associated with charge hopping and grain-boundary polarization when the characteristic relaxation time becomes comparable to the period of the applied field [65,66]. The loss tangent increased towards the peak as the polarization response lagged behind the applied field and energy dissipation increased. Beyond the peak the slower charge and dipole processes could no longer follow the field effectively and the loss decreased. HA showed the highest maximum tan δ of 3.2 compared with 1.9 for SrHA and 1.7 for FHA. Its higher loss may be related to hydroxyl-related defects and possible proton-conduction pathways. The substitution with Sr^{2+} or F^- may alter the mobility of these defects and reduce energy dissipation [68]. The relaxation peak of FHA occurred at a higher frequency than that of HA which may indicate a shorter relaxation time. SrHA showed a shift towards lower frequency that may be associated with Sr-induced lattice distortion and slower defect-dipole relaxation [68,69]. An additional high-frequency peak in SrHA and a shoulder in FHA may point to multiple relaxation processes involving dopant-related defects and localized ionic hopping. The broadened and asymmetric peaks are consistent with non-Debye relaxation behaviour [66,67].

The AC conductivity of HA, SrHA and FHA at 1 MHz was 6.7×10^{-6}, 1.2×10^{-5} and 2.3×10^{-5}, respectively. The conductivity remained nearly constant in the low-frequency plateau region, which is associated with long-range charge transport and the DC conductivity contribution. At higher frequencies the conductivity increased in accordance with the general behaviour described by Jonscher's universal power law. This increase may arise from charge carriers hopping between localized sites under the alternating electric field [62,65]. Both doped samples exhibited higher AC conductivity than HA. In SrHA this may be associated with lattice expansion and changes in defect-mediated transport [62,69]. FHA showed the highest conductivity which may involve charge transport along the apatite channels and changes in the local defect environment following fluoride substitution [61,66,67]. These interpretations require confirmation through temperature dependent conductivity measurements or impedance analysis.

The capacitance decreased with increasing frequency for all samples. At 1 Hz the capacitance of HA, SrHA and FHA was 8 nF, 22 nF and 31 nF, respectively. At 1 MHz, the values decreased to 4 pF, 6 pF and 14.9 pF. The higher low-frequency capacitance is associated with interfacial and dipolar polarization, which contribute more strongly when the applied field changes slowly [66,67,69]. As frequency increases these slower mechanisms contribute less and the capacitance decreases. At high frequencies the response becomes increasingly governed by faster polarization processes. The larger capacitance of SrHA and FHA relative to HA is consistent with their enhanced dielectric response. The higher AC conductivity of the doped samples may influence the measured electrical response through changes in charge transport and leakage [69]. These findings establish that Sr^{2+} and F^- substitution modifies

the dielectric loss and charge transport and capacitance of nanohydroxyapatite. Such changes are relevant to evaluating its use as a ceramic filler in triboelectric nanogenerators and other energy-harvesting systems

Measurement of electrical output: The triboelectric voltages recorded for HA and SrHA and FHA were 261 V, 275 V and 277 V, respectively. The corresponding currents were 9.2 μA, 11.23 μA and 12.8 μA (Table-3). The time-dependent open-circuit voltage and short-circuit current profiles of the PVA–HA and PVA–SrHA and PVA–FHA layers are shown in Figs. 9 and 10. The reference PVA–PTFE device generated a peak-to-peak voltage of 128 V and a current of 2.83 μA. The higher output of the HA-filled films indicates the contribution of the ceramic fillers to the triboelectric response. The comparable film thicknesses and preparation conditions were maintained across the devices. Incorporation of nanohydroxyapatite may enhance the dielectric response and surface roughness of PVA through its polar functional groups and improve interfacial charge storage [70].

TABLE-3
COMPARISON OF PEAK-TO-PEAK VOLTAGE AND CURRENT OUTPUTS FOR HA-BASED SAMPLES

Sample	Peak-to-peak voltage (V_{pp})	Peak-to-peak current (I_{pp})
HA	261	9.20
SrHA	275	11.23
FHA	277	12.80

The substitution of Sr^{2+} may increase lattice distortion and modify dipolar polarization and charge transport which is consistent with the higher voltage and current of SrHA compared with HA [71]. FHA exhibited the highest output with a voltage of 277 V and a current of 12.8 μA. This improvement may be associated with changes in lattice stability and local polarization following OH^- substitution by F^-. The altered surface charge distribution may support charge trapping and retention during repeated contact and separation [64,68]. Fluoride substitution may further influence interfacial charge transfer and contribute to the higher output of FHA [66,68,72]. These results show that ionic substitution modifies the electrical response of nanohydroxyapatite and supports its potential use as a ceramic filler in triboelectric nanogenerators.

Conclusion

This study establishes the successful synthesis of pure and strontium- and fluorine-doped nanohydroxyapatite and evaluates the effects of ionic substitution on their structural, dielectric and triboelectric properties. Strontium incorporation expanded the lattice and increased the crystallite size, whereas fluoride substitution contracted the *a*-axis and reduced the crystallite size. Fluoride-doped HA exhibited the lowest thermal mass loss, while both doped samples showed modified dielectric behaviour and higher AC conductivity than pure HA. The PVA-based TENG incorporating FHA achieved the highest electrical output, with a voltage of 277 V and a current of 12.8 μA, compared with 261 V and 9.2 μA for HA. These results establish that Sr^{2+} and F^- substitution can modify the electrical response of nanohydroxyapatite, with FHA showing the most promising output among the compositions investigated. The improved performance may be associated with changes in polarization, charge transport and interfacial charge accumulation, although these mechanisms require fur-

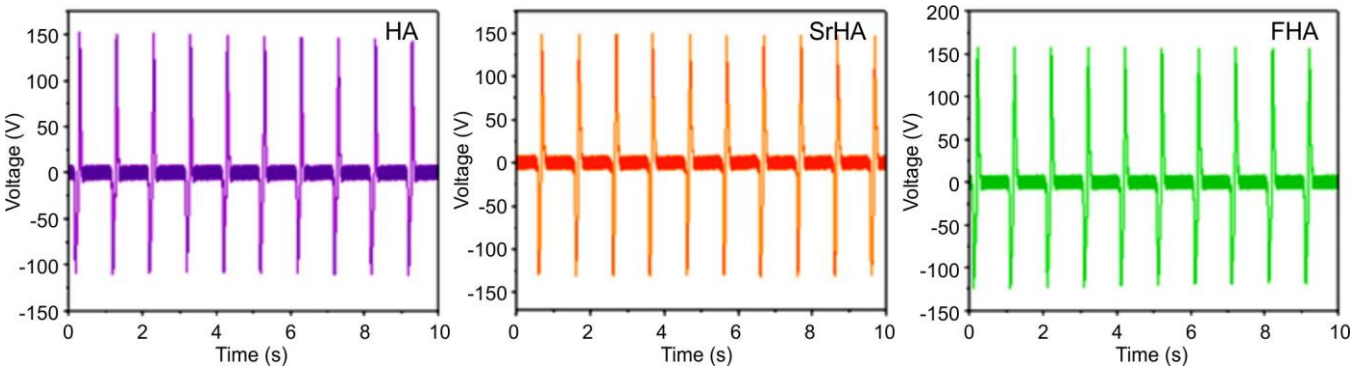


Fig. 9. Plots of time-dependent variation of open-circuit voltage for PVA-HA/SRHA/FHA layers

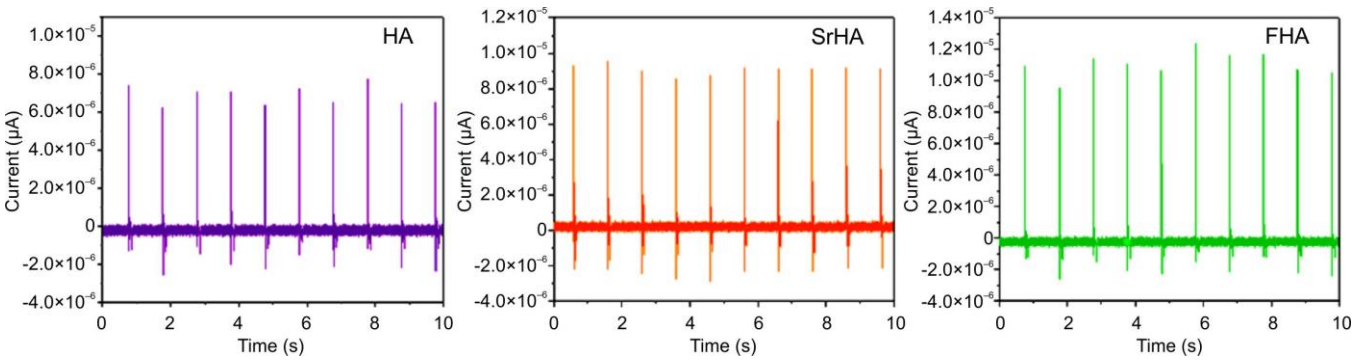


Fig. 10. Plots of time-dependent variation of short-circuit current for PVA-HA/SRHA/FHA layers

ther experimental verification. Since only one concentration of each dopant was examined, further studies should assess concentration-dependent effects, long-term operational stability, output reproducibility and performance under different mechanical conditions.

ACKNOWLEDGEMENTS

The authors thank the authorities of Sophisticated Analytical Instrumental Facilities (SAIF), Cochin University of Science and Technology and CLIF, University of Kerala, for providing advanced instrumental and analytical facilities. The authors also thank the Principals of M.G. College and the College of Engineering, Thiruvananthapuram, for providing the facilities to carry out this research.

CONFLICT OF INTEREST

The authors declare that there is no conflicts of interest regarding the publication of this article.

DECLARATION OF AI-ASSISTED TECHNOLOGIES

During the preparation of this manuscript, the authors used an AI-assisted tool(s) to improve the language and no data, results or scientific conclusions were generated by AI. All analyses, interpretations and conclusions are the authors' own. The authors reviewed and edited the content and take full responsibility for the published work.

REFERENCES

1. Z.L. Wang, *Nat. Rev. Mater.*, **5**, 773 (2020); https://doi.org/10.1038/s41578-020-0226-0
2. S.V. Dorozhkin, *Biomaterials*, **31**, 1465 (2010); https://doi.org/10.1016/j.biomaterials.2009.11.050
3. R.Z. LeGeros, *Chem. Rev.*, **108**, 4742 (2008); https://doi.org/10.1021/cr800427g
4. S.V. Dorozhkin, *Materials*, **6**, 3840 (2013); https://doi.org/10.3390/ma6093840
5. N.D. Ravi, R. Balu and T.S. Sampath Kumar, *J. Am. Ceram. Soc.*, **95**, 2700 (2012); https://doi.org/10.1111/j.1551-2916.2012.05262.x
6. Z.L. Wang, *Mater. Today*, **20**, 74 (2017); https://doi.org/10.1016/j.mattod.2016.12.001
7. S. Wang, W. Tong, Y. Li, P. Zhang, Y. Liu, Y. Chen and Y. Zhang, *Nano Energy*, **105**, 108026 (2023); https://doi.org/10.1016/j.nanoen.2022.108026
8. X. Cheng, W. Tang, Y. Song, H. Chen, H. Zhang and Z.L. Wang, *Nano Energy*, **61**, 517 (2019); https://doi.org/10.1016/j.nanoen.2019.04.096
9. C. Capuccini, P. Torricelli, F. Sima, E. Boanini, C. Ristoscu, B. Bracci, G. Socol, M. Fini, I.N. Mihailescu and A. Bigi, *Acta Biomater.*, **4**, 1885 (2008); https://doi.org/10.1016/j.actbio.2008.05.005
10. T. Nagyné-Kovács, L. Studnicka, A. Kincses, G. Spengler, M. Molnár, M. Tolner, I.E. Lukács, I.M. Szilágyi and G. Pokol, *Ceram. Int.*, **44**, 22976 (2018); https://doi.org/10.1016/j.ceramint.2018.09.096
11. H. Eslami, M. Solati-Hashjin and M. Tahriri, *Mater. Sci. Eng. C*, **29**, 1387 (2009); https://doi.org/10.1016/j.msec.2008.10.033
12. I. Uysal, F. Severcan, A. Tezcaner and Z. Evis, *Prog. Nat. Sci.*, **24**, 340 (2014); https://doi.org/10.1016/j.pnsc.2014.06.004
13. H. Qu and M. Wei, *Acta Biomater.*, **2**, 113 (2006); https://doi.org/10.1016/j.actbio.2005.09.003
14. C.M. Mardziah, I. Sopyan, M. Hamdi and S. Ramesh, *Med. J. Malaysia*, **63(Suppl. A)**, 79 (2008).
15. P. Nasker, M. Mukherjee, S. Kant, S. Tripathy, A. Sinha and M. Das, *Ceram. Int.*, **44**, 22008 (2018); https://doi.org/10.1016/j.ceramint.2018.07.175
16. A. Afshar, M. Ghorbani, N. Ehsani, M.R. Saeri and C.C. Sorrell, *Mater. Des.*, **24**, 197 (2003); https://doi.org/10.1016/S0261-3069(03)00003-7
17. S. Koutsopoulos, *J. Biomed. Mater. Res.*, **62**, 600 (2002); https://doi.org/10.1002/jbm.10280
18. M. Sadat-Shojai, M.T. Khorasani, E. Dinpanah-Khoshdargi and A. Jamshidi, *Acta Biomater.*, **9**, 7591 (2013); https://doi.org/10.1016/j.actbio.2013.04.012
19. L. Stipniece, K. Salma-Ancane, D. Loca and S. Pastare, *Key Eng. Mater.*, **674**, 3 (2016); https://doi.org/10.4028/www.scientific.net/KEM.674.3
20. M.P. Moreira, G.D. de Almeida Soares, J. Dentzer, K. Anselme, L.Á. de Sena, A. Kuznetsov and E.A. dos Santos, *Mater. Sci. Eng. C*, **61**, 736 (2016); https://doi.org/10.1016/j.msec.2016.01.004
21. L.L. Dai, F. Nudelman, C.H. Chu, E.C.M. Lo and M.L. Mei, *J. Dent.*, **105**, 103581 (2021); https://doi.org/10.1016/j.jdent.2021.103581
22. A. Rajabnejadkeleshteri, A. Kamyar, M. Khakbiz, Z.L. Bakalani and H. Basiri, *Microchem. J.*, **153**, 104485 (2020); https://doi.org/10.1016/j.microc.2019.104485
23. S. Yempally, S. Bonthula and D. Ponnamma, *Mater. Renew. Sustain. Energy*, **13**, 265 (2024); https://doi.org/10.1007/s40243-024-00264-9
24. S.R. Gopal, T.S. Velayutham, W.C. Gan, J.Y. Cheong and A.E. Soh, *RSC Adv.*, **13**, 7921 (2023); https://doi.org/10.1039/D3RA00077J
25. A.K. Swami and D. Verma, *Sci. Rep.*, **16**, 22421 (2026); https://doi.org/10.1038/s41598-026-53128-9
26. L.V. Anitha Rani, N. Abraham, S. Rani, A. Satheesan and R. Rajendran, *Prog. Org. Coat.*, **211**, 109773 (2026); https://doi.org/10.1016/j.porgcoat.2025.109773
27. M.H. Fathi, A. Hanifi and V. Mortazavi, *J. Mater. Process. Technol.*, **202**, 536 (2008); https://doi.org/10.1016/j.jmatprotec.2007.10.004
28. L. Li, H. Pan, J. Tao, X. Xu, C. Mao, X. Gu and R. Tang, *J. Mater. Chem.*, **18**, 4079 (2008); https://doi.org/10.1039/b806090h
29. M. Vallet-Regí and J.M. González-Calbet, *Prog. Solid State Chem.*, **32**, 1 (2004); https://doi.org/10.1016/j.progsolidstchem.2004.07.001
30. M.D. O'Donnell, Y. Fredholm, A. de Rouffignac and R.G. Hill, *Acta Biomater.*, **4**, 1455 (2008); https://doi.org/10.1016/j.actbio.2008.04.018
31. W.-H. Ren, S. Xin, K. Yang, Y.-B. Yu, S.-M. Li, J.-J. Zheng, K. Huang, R.-C. Zeng, X.-X. Yang, L. Gao, S.-Q. Li and K. Zhi, *Adv. NanoBiomed Res.*, **2**, 2200018 (2022); https://doi.org/10.1002/anbr.202200018
32. L.M. Rodríguez-Lorenzo, J.N. Hart and K.A. Gross, *Biomaterials*, **24**, 3777 (2003); https://doi.org/10.1016/S0142-9612(03)00259-X
33. J.C. Elliott, Structure and Chemistry of the Apatites and Other Calcium Orthophosphates, Elsevier, Amsterdam (1994).
34. V.L. Snoeyink and D. Jenkins, Water Chemistry, John Wiley & Sons, New York (1980).
35. R.D. Shannon, *Acta Crystallogr. A*, **32**, 751 (1976); https://doi.org/10.1107/S0567739476001551
36. J. Kolmas, E. Groszyk and D. Kwiatkowska-Różycka, *BioMed Res. Int.*, **2014**, 178123 (2014); https://doi.org/10.1155/2014/178123
37. L. Rintoul, E. Wentrup-Byrne, S. Suzuki and L. Grøndahl, *J. Mater. Sci. Mater. Med.*, **18**, 1701 (2007); https://doi.org/10.1007/s10856-007-3052-3
38. K. Nakamoto, Infrared and Raman Spectra of Inorganic and Coordination Compounds, edn 6, Wiley, New York (2009).
39. I. Rehman and W. Bonfield, *J. Mater. Sci. Mater. Med.*, **8**, 1 (1997); https://doi.org/10.1023/A:1018570213546

40. M. Zang, L. Li, X. Sun, Z. Niu, X. Bai and X. Liu, *J. Mech. Behav. Biomed. Mater.*, **151**, 106364 (2024); https://doi.org/10.1016/j.jmbbm.2023.106364
41. A. Ślósarczyk, Z. Paszkiewicz and C. Paluszkiewicz, *J. Mol. Struct.*, **744-747**, 657 (2005); https://doi.org/10.1016/j.molstruc.2004.11.078
42. E. Landi, G. Celotti, G. Logroscino and A. Tampieri, *J. Eur. Ceram. Soc.*, **23**, 2931 (2003); https://doi.org/10.1016/S0955-2219(03)00304-2
43. M. Frasnelli, F. Cristofaro, V.M. Sglavo, S. Dirè, E. Callone, R. Ceccato, G. Bruni, A.I. Cornaglia and L. Visai, *Mater. Sci. Eng. C*, **71**, 653 (2017); https://doi.org/10.1016/j.msec.2016.10.047
44. M. De, S. Hajra, R. Tiwari, S. Sahoo, R.N.P. Choudhary and H.S. Tewari, *Ceram. Int.*, **44**, 11792 (2018); https://doi.org/10.1016/j.ceramint.2018.03.263
45. N.V. Bulina, S.V. Makarova, A.A. Matvienko, K.B. Gerasimov, S.G. Baev, O.A. Logutenko and V.S. Bystrov, *Minerals*, **11**, 1310 (2021); https://doi.org/10.3390/min11121310
46. S.J. Kalita, A. Bhardwaj and H.A. Bhatt, *Mater. Sci. Eng. C*, **27**, 441 (2007); https://doi.org/10.1016/j.msec.2006.05.018
47. R.V. Suganthi, K. Elayaraja, M.I.A. Joshy, V.S. Chandra, E.K. Girija and S.N. Kalkura, *Mater. Sci. Eng. C*, **31**, 593 (2011); https://doi.org/10.1016/j.msec.2010.11.025
48. D. Tadić and M. Epple, *Biomaterials*, **25**, 987 (2004); https://doi.org/10.1016/S0142-9612(03)00621-5
49. K.M. Balabadra, S. Panneer Selvam, R. Ramadoss and S. Sundar, *J. Oral Biol. Craniofac. Res.*, **14**, 706 (2024); https://doi.org/10.1016/j.jobcr.2024.09.009
50. L.O. Ahmed and R.A. Omer, *Rev. Inorg. Chem.*, **44**, 599 (2024); https://doi.org/10.1515/revic-2024-0018
51. M. He, Z. Zhang, M. Wang, C. Liang, H. Wang, C. Cheng, Y. Li, Y. Wang and Z. Zhang, *J. Hazard. Mater.*, **481**, 136525 (2025); https://doi.org/10.1016/j.jhazmat.2024.136525
52. L.T. Bang, N.V. Ha, B.D. Long and N.T. Hong Nhung, *Vietnam J. Sci. Technol.*, **63**, 897 (2024); https://doi.org/10.15625/2525-2518/18533
53. S. Shaikh, S. Mehrotra, B. van Bochove, A.K. Teotia, P. Singh, I. Laurén, N.C. Lindfors, J. Seppälä and A. Kumar, *ACS Appl. Mater. Interfaces*, **16**, 65378 (2024); https://doi.org/10.1021/acsami.4c16195
54. W. Du, Y. Yang, J. Liu, Y. Zhu, T. Shen, Q. Chen and T. Miyazaki, *ACS Biomater. Sci. Eng.*, **10**, 6874 (2024); https://doi.org/10.1021/acsbiomaterials.4c00306
55. M. Wang, H.-Y. Zhang, Y.-Y. Xiang, Y.-P. Qian, J.-N. Ren and R. Jia, *Appl. Surf. Sci.*, **586**, 152753 (2022); https://doi.org/10.1016/j.apsusc.2022.152753
56. M. Kaur, S. Shahid, N. Karpukhina, P. Anderson and F.S.L. Wong, *Front. Oral Health*, **5**, 1332298 (2024); https://doi.org/10.3389/froh.2024.1332298
57. Y. Zou, Y. Wang, J. Wang, S. Wang, L. Chen, Y. Xi, R. Xie, J. Yang and X. Xiao, *RSC Adv.*, **14**, 26103 (2024); https://doi.org/10.1039/D4RA02147A
58. A. Szcześ, L. Hołysz and E. Chibowski, *Adv. Colloid Interface Sci.*, **249**, 321 (2017); https://doi.org/10.1016/j.cis.2017.04.007
59. N. Eliaz and N. Metoki, *Materials*, **10**, 334 (2017); https://doi.org/10.3390/ma10040334
60. A. Valanezhad, T. Odatsu, K. Udoh, T. Shiraishi, T. Sawase and I. Watanabe, *J. Mater. Sci. Mater. Med.*, **27**, 3 (2016); https://doi.org/10.1007/s10856-015-5614-0
61. A.K. Jonscher, *Nature*, **267**, 673 (1977); https://doi.org/10.1038/267673a0
62. M. Mahardika, N. Masruchin, D. Amelia, R.A. Ilyas, A.A. Septevani, E. Syafri, N. Hastuti, M. Karina, M.A. Khan, B.-H. Jeon and N.H. Sari, *RSC Adv.*, **14**, 23232 (2024); https://doi.org/10.1039/D4RA04205K
63. F. Rashid, S.S. Soshi and M.A. Gafur, *Mater. Sci. Appl.*, **15**, 336 (2024); https://doi.org/10.4236/msa.2024.159023
64. M. Kawsar, M. Sahadat Hossain, S. Tabassum, D. Islam, N.M. Bahadur and S. Ahmed, *RSC Adv.*, **14**, 29665 (2024); https://doi.org/10.1039/D4RA03111C
65. R. Gupta and S. Agrawal, *Chem. Phys. Impact*, **9**, 100668 (2024); https://doi.org/10.1016/j.chphi.2024.100668
66. N. Horiuchi, J. Endo, K. Nozaki, M. Nakamura, K. Katayama, A. Nagai, and K. Yamashita, *J. Ceram. Soc. Jpn.*, **121**, 770 (2013); https://doi.org/10.2109/jcersj2.121.770
67. A. Laghzizil, N. El Herch, A. Bouhaouss, G. Lorente and J. Macquete, *J. Solid State Chem.*, **156**, 57 (2001); https://doi.org/10.1006/jssc.2000.8958
68. S. Mary Stella and U. Vijayalakshmi, *Asian J. Chem.*, **35**, 1361 (2023); https://doi.org/10.14233/ajchem.2023.27741
69. K.P. Tank, B.V. Jogiya, D.K. Kanchan and M.J. Joshi, *Diffus. Defect Data Solid State Data Pt. B Solid State Phenom.*, **209**, 151 (2013); https://doi.org/10.4028/www.scientific.net/SSP.209.151
70. T.T. Luu, N.D. Huynh, H. Kim, Z.-H. Lin and D. Choi, *Nanoscale*, **15**, 14205 (2023); https://doi.org/10.1039/D3NR02849F
71. T. Das, B.K. Das, K. Parashar, R. Kumar, H.K. Choudhary, A.V. Anupama, B. Sahoo, P.K. Sahoo and S.K.S. Parashar, *J. Mater. Sci. Mater. Electron.*, **28**, 13587 (2017); https://doi.org/10.1007/s10854-017-7198-6
72. X. Li, Q. Yang, D. Ren, Q. Li, H. Yang, X. Zhang and Y. Xi, *Nanoscale Adv.*, **6**, 4522 (2024); https://doi.org/10.1039/D4NA00340C